# Accurate simulation of near-wall turbulence over a compliant tensegrity fabric

Haoxiang Luo\* and Thomas R. Bewley
Flow Control Lab, Dept. of MAE, UC San Diego, La Jolla, CA 92093-0411, USA

#### **ABSTRACT**

This paper presents a new class of compliant surfaces, dubbed *tensegrity fabrics*, for the problem of reducing the drag induced by near-wall turbulent flows. The substructure upon which this compliant surface is built is based on the "tensegrity" structural paradigm, and is formed as a stable pretensioned network of compressive members ("bars") interconnected by tensile members ("tendons"). Compared with existing compliant surface studies, most of which are based on spring-supported plates or membranes, tensegrity fabrics appear to be better configured to respond to the shear stress fluctuations (in addition to the pressure fluctuations) generated by near-wall turbulence. As a result, once the several parameters affecting the compliance characteristics of the structure are tuned appropriately, the tensegrity fabric might exhibit an improved capacity for dampening the fluctuations of near-wall turbulence, thereby reducing drag.

This paper improves our previous work (SPIE Paper 5049-57) and uses a 3D time-dependent coordinate transformation in the flow simulations to account for the motion of the channel walls, and the Cartesian components of the velocity are used as the flow variables. For the spatial discretization, a dealiased pseudospectral scheme is used in the homogeneous directions and a second-order finite difference scheme is used in the wall-normal direction. The code is first validated with several benchmark results that are available in the published literature for flows past both stationary and nonstationary walls. Direct numerical simulations of turbulent flows at  $Re_{\tau} = 150$  over the compliant tensegrity fabric are then presented. It is found that, when the stiffness, mass, damping, and orientation of the members of the turbulence are altered significantly. The flow/structure interface is found to form streamwise-travelling waves reminiscent of those found at air-water interfaces, but traveling at a faster phase velocity. Under certain conditions, the coupled flow/structure system is found to resonate, exhibiting a synchronized, almost sinusoidal interfacial motion with relatively long streamwise correlation.

# 1. INTRODUCTION

Dominated by so-called "coherent structures" (that is, distinctive vortices with characteristic statistics that evolve in a chaotic fashion), near-wall turbulence is responsible for significant drag penalties in many flows of engineering relevance. Many ideas have been explored in various attempts to attenuate turbulence near walls to improve system efficiency. Among them, the use of compliant surfaces is one of the most attractive, as this approach requires no control inputs and is quite simple in concept: the structure is allowed to flex in response to the fluctuations of the near-wall turbulence, thereby allowing the energy of the turbulent fluctuations to be transmitted into the structure, where it may be damped out. By reducing the intensity of the fluctuations of near-wall turbulence in this manner (if this effect can be realized), presumably turbulence-induced drag might also be reduced.

However, perhaps due largely to a lack of theoretical insight into the choice of an appropriate compliant material, most experiments to date have failed to establish the hypothesis that turbulence-induced drag can in fact be reduced by compliant surfaces. Comprehensive reviews and comments about the long history of related experiments may be found in Bushnell, Hefner & Ash (1977), Carpenter & Garrad (1985) and Gad-el Hak (1986, 1987, 1996). Despite several unsuccessful experimental trials, two recent exceptions in the literature are worth noting: Lee, Fisher & Schwarz (1993) observed a significant reduction of turbulent intensity in their experiments of boundary layers over compliant surfaces, and Choi *et al.* (1997) claimed up to 7% drag reduction and up to 5% reduction of turbulent intensity across almost the entire turbulent boundary layer in their experiments, apparently due to the effect of a compliant surface.

Though results are mixed in the fully turbulent regime, compliant surfaces have a well-established capability to delay laminar-to-turbulent transition. This has been studied analytically by many investigators using linear stability theory

<sup>\*</sup>hluo@ucsd.edu; phone 1 858 822-3729; fax 1 858 822-3107

(Benjamin, 1960; Landahl, 1962; Carpenter & Garrad, 1985; Carpenter & Morris, 1990; Davies & Carpenter, 1997), and has been confirmed in experiments (Daniel *et al.*, 1987; Gaster, 1988). Some hypothesize that the efficient swimming capability of the bottle-nosed dolphin might be due, at least in part, to the transition delay caused by its compliant skin (see, e.g., Carpenter, Davies & Lucey, 2000). Unfortunately, the linear stability theory that has shed so much light on the compliant surface problem in the transitional regime fails to provide much useful guidance in the turbulent regime, where we must instead resort to other tools, such as numerical simulation.

As computers continue to become more powerful and numerical simulation tools continue to become more efficient and accurate, we can begin to address the compliant surface problem in the turbulent regime numerically. Prior work in this area is mostly quite recent. Endo & Himeno (2002) performed a direct numerical simulation of turbulence over a compliant surface and reported approximately 2 to 3% drag reduction. However, their result was soon challenged by Xu, Rempfer & Lumley (2003) for the reason of insufficient averaging time. In the simulations of Xu et al., no drag reduction was found; in fact, wall compliance had no statistically significant effect on the turbulent boundary layer whatsoever. In both papers, the rms displacement and velocity of the wall motion,  $y_{w,rms}$  and  $v_{w,rms}$ , are quite small. In Endo & Himeno,  $y_{w,rms}^+$  is about 0.008 and  $v_{w,rms}^+$  is about 0.025. In Xu et al., we estimate from their figures that  $y_{w,rms}^+$  is about 0.05 and  $v_{w.rms}^+$  is about 0.01. It is, indeed, improbable that such small wall motions can have a significant influence on the statistics of the turbulence, as the length scales of the energetic motions of the coherent structures are much larger. The models used for the compliant surface in both of these papers are generalizations of the spring-supported thin plate model proposed by Carpenter & Garrad (1985). Governed by a simple linear PDE, this type of model is convenient for theoretical analyses in laminar flows. However, this surface model responds only to the normal load (that is, pressure fluctuations), not to the tangential load (skin friction fluctuations). As skin-friction fluctuations are related to the first-order terms of the Taylor series expansion of the velocity fluctuations near the wall, whereas pressure fluctuations are related to higher-order terms (see, e.g., Bewley & Protas, 2004), one might hypothesize that the surface response to the skin friction fluctuations of the flow should at least be comparable, in some averaged sense, to the surface response to the pressure fluctuations of the flow. In other words, a compliant surface, such as the tensegrity fabric, that can respond to both kinds of loads might present certain advantages. Motivated by this hypothesis, we have focused on tensegrity fabrics exclusively in this work.

As mentioned in the abstract, the truss paradigm known as *tensegrity* is a stable pretensioned collection of structural members always either under tension ("tendons") or compression ("bars"); no individual structural member ever experiences bending moments. Such structures are often particularly mass efficient for bearing loads. The same structural paradigm appears to form the molecular foundation for spider fibers (Ingber, 1997, 1998), which is nature's strongest material per unit mass (several times stronger per unit mass than steel). In contrast with the spring-supported plate model, the tensegrity fabric is an inherently discrete structure with a relatively involved topology. However, the calculation of the dynamics of the present tensegrity structure is straightforward when framed appropriately, as discussed in detail in Luo & Bewley (2003) and Luo & Bewley (2005).

Note that, with this work, we are *not* proposing tensegrity as a new model for viscoelastic materials such as a rubber coating. Instead, we are exploring the possible development of an altogether new class of compliant surfaces. If our computations show that this type of compliant surface holds promise for exhibiting drag reducing capabilities, we will then explore the manufacturability of appropriately tuned tensegrity fabrics via extensions of existing textile technologies, incorporating compressive elements into the weave.

#### 2. GOVERNING EQUATION

# 2.1. Coordinate transformation

To accommodate the interface motion of the flow, we previously investigated the potential use of the immersed boundary method (Luo & Bewley, 2003). In the immersed boundary method, the flow domain is extended to immerse the irregular interface, a Cartesian grid is used over this entire extended domain, and a fictitious force is applied to the "flow" outside the physical part of the flow domain in order to bring the flow to rest (actually, to bring the flow to a velocity that matches the wall velocity) at the location of the irregular interface defining the actual flow boundary. In comparison with the coordinate transformation method, the immersed boundary method is fairly simple, as the numerical grid remains fixed in physical coordinates even as the walls flex. However, when applied in a pseudospectral flow simulation code, as used in the present work, the immersed boundary method was found to represent accurately only the effects of very small wall deformations. When larger deformations (greater than the wall-normal grid spacing at the wall) were present, the forcing applied by

Proc. of SPIE Vol. 5757 185

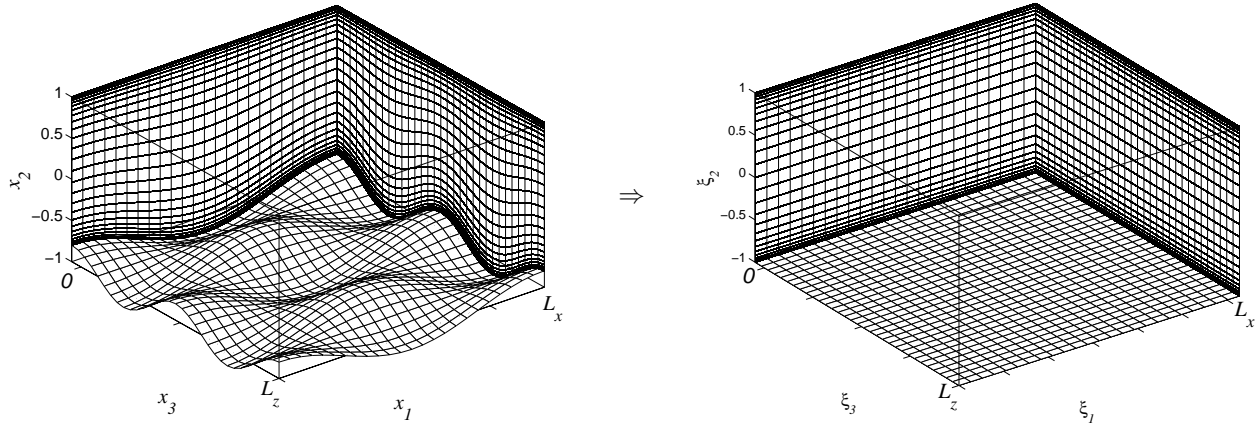


Figure 1. Domain transformation.

the immersed boundary method at the gridpoints just outside the physical part of the domain typically triggered Gibbs phenomenon, exciting small-scale fluctuations that grew and eventually destabilized the nonlinear simulation. Therefore, in this paper we improve the accuracy of the simulations by adopting the coordinate transformation method where the time-dependent boundary-conforming grid allows better resolution in the near-wall region.

Defining  $\eta_u(x_1, x_3, t)$  and  $\eta_l(x_1, x_3, t)$  as the upper and lower wall displacements in the wall-normal direction from the respective nominal positions of the walls  $(x_2 = \pm 1)$ , and defining  $\eta_1 = (\eta_u - \eta_l)/2$  and  $\eta_0 = (\eta_u + \eta_l)/2$ , the following time-dependent coordinate transformation may be used to map the irregular physical domain into a rectangular domain

$$x_1 = \xi_1, \quad x_2 = \xi_2(1 + \eta_1) + \eta_0, \quad x_3 = \xi_3, \quad t = t,$$
 (1)

where  $x_i$  denotes the Cartesian coordinates and  $\xi_i$  denotes the curvilinear coordinates. This domain transformation is illustrated in Figure 1. Note that the code developed in this work allows both walls to deform, though only the lower wall is deformed in the main compliant surface simulations reported in §5, as illustrated in Figure 1. Note also that we use the variables  $\{x,y,z\}$  and  $\{x_1,x_2,x_3\}$  interchangably to denote the streamwise, wall-normal, and spanwise directions. The nominal domain size is  $L_x \times L_y \times L_z$ , where  $L_x$  and  $L_z$  are identified in the sections to follow and  $L_y = 2$ .

The incompressible Navier-Stokes equation that governs the flow system is

$$\frac{\partial u_i}{\partial t} + \frac{\partial u_j u_i}{\partial x_j} = -\frac{1}{\rho} \frac{\partial p}{\partial x_i} + \nu \frac{\partial^2 u_i}{\partial x_j^2} - \delta_{i1} P_x, 
\frac{\partial u_j}{\partial x_j} = 0,$$
(2)

where  $\rho$  is the (constant) density, p is the hydrodynamic pressure, and v is the kinetic viscosity. Distances  $x_i$  are normalized by the half-width of the channel h, velocities  $u_i$  are normalized by the mean friction velocity  $u_\tau$  of the corresponding turbulent channel flow with solid walls, and time t is normalized by  $h/u_\tau$ . (Note that, where explicitly specified, the scaling is different for some of the code validation tests in §3.) The spatially-uniform pressure gradient in the  $x_1$  diection,  $P_x$ , is adjusted in time to maintain constant mass flux in the physical domain. The determinant of the Jacobian matrix of the transformation is given by  $J = \left| \frac{\partial x}{\partial \xi} \right| = \frac{\partial x_2}{\partial \xi_2}$ .

Defining the nontrivial elements of the transformation as

$$\varphi_i = \frac{\partial \xi_2}{\partial x_i}, \qquad \qquad \varphi_{\tau} = \frac{\partial \xi_2}{\partial t},$$

we may apply the chain rules to substitute the derivatives in (2) and to express the equation in terms of the new coordinates.

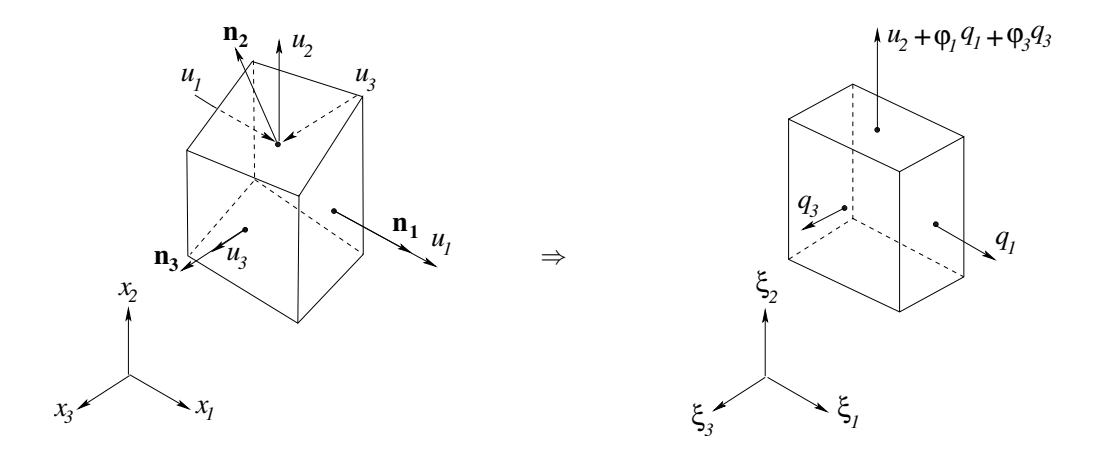


Figure 2. Cell transformation.

## 2.2. Choice of dependent variables

Velocity vectors in a curvilinear coordinate system may be defined as Cartesian vectors, whose bases are associated with the original  $(\mathbf{x})$  coordinates, or contravariant vectors, whose bases are associated with the deformed  $(\mathbf{\xi})$  coordinates. In either case, multiplying the Navier-Stokes equation by the transformation Jacobian determinant J results in a governing equation in a strong conservation form which is favorable (for the purpose of momentum conservation) in numerical codes. However, using the contravariant form generally involves several additional terms to achieve the correct expression of both the temporal and spatial derivatives in a moving coordinate system; for further discussion of this approach, see Luo & Bewley (2004). The contravariant formulation thus renders the governing equation more involved and expensive to solve even in a relatively simple flow such as the present, in which the transformation only affects the wall-normal coordinate. In this work, therefore, we choose to represent the velocity vectors in Cartesian form, thereby simplifying the computation significantly.

To understand our choice of primitive variables, consider the problem of mass conservation from finite volume point of view. Figure 2 illustrates the transformation of a single computational cell. In the transformation used in this work, the vertical grid lines are not deformed by the transformation. As a result, among 6 faces of the cell indicated, only top face and bottom face have their surface normals inclined from the corresponding cartesian basis vectors. Horizontal flow ( $u_1$  or  $u_3$ , in the  $u_1$  or  $u_3$  direction) will cause fluid to pass through both of these faces. When considering the conservation of mass in this cell, we may assume that all of its faces are stationary, as the effects of the cell's motion are taken into account in the geometrical conservation law (see Rosenfeld & Kwak, 1991), which is satisfied by the analytical coordinate transformation (1). Thus, in the case of the top face (whose surface normal is  $u_2$ ), the volume flux out of the cell is

$$\mathbf{u} \cdot \mathbf{n}_{2} = \mathbf{u} \cdot \left(\frac{\partial \mathbf{x}}{\partial \xi_{3}} d\xi_{3} \times \frac{\partial \mathbf{x}}{\partial \xi_{1}} d\xi_{1}\right) = \begin{pmatrix} u_{1} \\ u_{2} \\ u_{3} \end{pmatrix} \cdot \begin{pmatrix} -\frac{\partial x_{2}}{\partial \xi_{1}} \\ 1 \\ -\frac{\partial x_{2}}{\partial \xi_{3}} \end{pmatrix} d\xi_{3} d\xi_{1} = \begin{pmatrix} u_{1} \\ u_{2} \\ u_{3} \end{pmatrix} \cdot \begin{pmatrix} J\phi_{1} \\ 1 \\ J\phi_{3} \end{pmatrix} d\xi_{3} d\xi_{1}$$
$$= (\phi_{1}Ju_{1} + u_{2} + \phi_{3}Ju_{3})d\xi_{3} d\xi_{1},$$

where  $\times$  denotes the cross product. Similarly, the volume flux through the positive  $x_1$  and  $x_3$  faces are

$$\mathbf{u} \cdot \mathbf{n}_1 = \mathbf{u} \cdot (\frac{\partial \mathbf{x}}{\partial \xi_2} d\xi_2 \times \frac{\partial \mathbf{x}}{\partial \xi_3} d\xi_3) = \frac{\partial x_2}{\partial \xi_2} u_1 d\xi_2 d\xi_3 = Ju_1 d\xi_2 d\xi_3,$$

$$\mathbf{u} \cdot \mathbf{n}_3 = \mathbf{u} \cdot (\frac{\partial \mathbf{x}}{\partial \xi_1} d\xi_1 \times \frac{\partial \mathbf{x}}{\partial \xi_2} d\xi_2) = \frac{\partial x_2}{\partial \xi_2} u_3 d\xi_1 d\xi_2 = Ju_3 d\xi_1 d\xi_2.$$

To summarize, the volume flux through these three faces are  $Ju_1$  in the  $\xi_1$  direction,  $u_2 + \varphi_1 Ju_1 + \varphi_3 Ju_3$  in the  $\xi_2$  direction, and  $Ju_3$  in the  $\xi_3$  direction; the volume flux through the opposite three faces are analogous. Note that these three

components form a vector which equals to the contravariant velocity vector in the curvilinear coordinates multiplied by the volume dilatation factor J. To avoid using such a contravariant vector for the reason of simplicity as described previously, and additionally avoiding the repeated application of this volume dilitation factor in the numerical code, we define the following Cartesian vector

$$q_1 = Ju_1, \quad q_2 = u_2, \quad q_3 = Ju_3$$
 (3)

and the modified pressure  $\tilde{p} = Jp/\rho$  as the primitive variables in our numerical code. As a consequence, the  $q_1$ - and  $q_3$ momentum equations are represented in strong conservation form due to their weighting by J. Requiring the net mass flux
into each cell be zero, we may write the continuity equation for this system as

$$D(q_i) = \frac{\partial q_1}{\partial \xi_1} + \frac{\partial (\varphi_1 q_1 + q_2 + \varphi_3 q_3)}{\partial \xi_2} + \frac{\partial q_3}{\partial \xi_3} = 0, \tag{4}$$

where  $D(\cdot)$  denotes the divergence operator.

The momentum equation in the new coordinates may now be written as

$$\frac{\partial q_i}{\partial t} + T_i(q_i) + N_i(q_j) = -G_i(\tilde{p}) + \nu L_i(q_i) - J P_x \delta_{i1}, \tag{5}$$

where  $T_i(q_i)$  is the term associated with the motion of the coordinates,  $N_i(q_j)$  is the convection term,  $G_i(\tilde{p})$  is the pressure term, and  $L_i(q_i)$  is the viscous term.

To maintain a constant bulk velocity  $U_{bulk}$ , the necessary spatially-uniform streamwise pressure gradient  $P_x$  is computed by integrating the  $u_1$  momentum equation over the entire physical domain,

$$U_{bulk} = \frac{1}{2L_x L_z} \int_0^{L_x} \int_0^{L_z} \int_{-1+\eta_l}^{1+\eta_u} u_1 dx_2 dx_3 dx_1 = \text{constant}$$

$$\Rightarrow P_x = \frac{1}{2 \int \int J d\xi_1 d\xi_3} \int \int \left[ -\varphi_1 \tilde{p} + \nu \varphi_1 \frac{\partial \varphi_1 q_1}{\partial \xi_2} + \nu \varphi_2 \frac{\partial q_1}{\partial \xi_2} + \nu \varphi_3 \frac{\partial \varphi_3 q_1}{\partial \xi_2} \right]_{\xi_2 = -1}^{\xi_2 = 1} d\xi_1 d\xi_3.$$
(6)

Periodic boundary conditions are assumed in the streamwise direction  $(\xi_1)$  and spanwise direction  $(\xi_3)$  for the dependent variables,  $\{q_1,q_2,q_3,\tilde{p}\}$ , and the wall deformation functions,  $\{\eta_u,\eta_l\}$ . No-slip and no-penetration boundary conditions are assumed at the two walls.

The numerical algorithm used for solving the unsteady incompressible Navier-Stokes equation in this work is based closely on that in Bewley, Moin & Temam (2001), in which the flow in a rectangular channel is controlled by unsteady wall-normal blowing and suction. As in that work, a hybrid pseudospectral / finite-difference method is used for the spatial discretization, and a mixed Crank-Nicolson / 3rd-order Runge-Kutta method is used for the temporal discretization. Several additional considerations are necessary in present work, however, as the governing equation is considerably more involved due to the coordinate transformation that accounts for the moving boundaries. In addition to the flow variables, the geometry-related time-varying coefficients,  $\varphi_i$  and  $\varphi_\tau$ , need to be spatially discretized. Further, not all terms involving derivatives in the wall-normal ( $\xi_2$ ) direction can be treated implicitly, as was possible in Bewley *et al.* (2001). For example, the terms with cross derivatives in the wall-normal direction and in one of the homogeneous directions ( $\xi_1$  or  $\xi_3$ ) must be treated explicitly. In addition, since the various Fourier modes can not be fully decoupled in the evaluation of the Laplacian, the pressure equation needs to be solved iteratively, subject to a boundary condition that is derived by imposing the incompressibility condition at the (possibly moving) walls. These issues are discussed in detail in Luo & Bewley (2005).

## 3. CODE VALIDATION

In order to validate our numerical algorithm, we applied the code to reproduce several existing results in the published literature for both laminar and turbulent channels flows with both stationary and moving walls. The full tests may be found in Luo & Bewley (2005). In summary, all the comparisons were done quantatitively and showed that our code is sufficiently accurate for the present compliant surface simulation. Due to constraint of space, we present here only one test and show the comparisons.

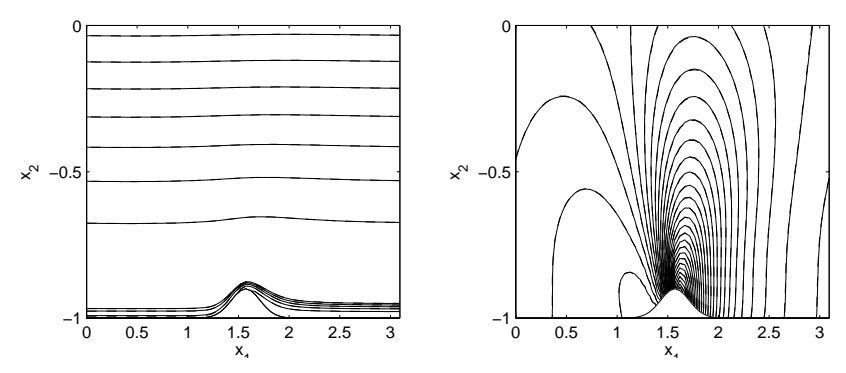


**Figure 3.** Flow at Re = 200 passing over an oscillating Gaussian bump uniform in the spanwise direction with the oscillation frequency  $\omega = 0.5$  at  $t = 3.0 h/U_c$ . Left: instantaneous streamlines  $\psi$ ; right: pressure contours. Solid: present simulation; dashed: results from Luo & Bewley (2004).

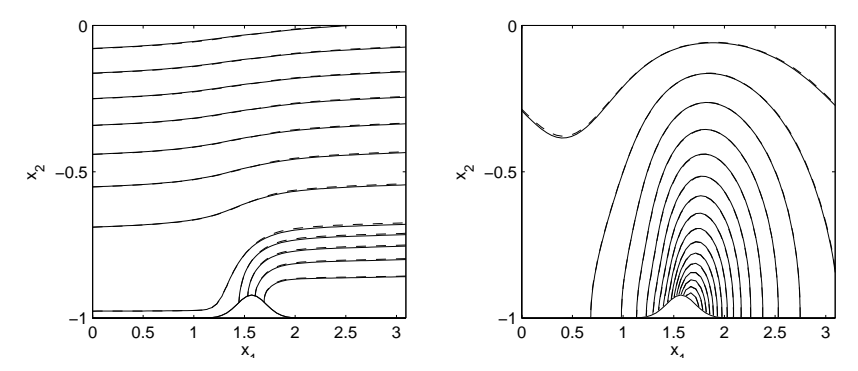


**Figure 4.** Flow at Re = 200 passing over an oscillating Gaussian bump uniform in the spanwise direction with the oscillation frequency  $\omega = 4$  at  $t = 1.8h/U_c$ . Left: instantaneous streamlines  $\psi$ ; right: pressure contours. Solid: present simulation; dashed: results from Luo & Bewley (2004).

In this test, we consider a (2D) flow with a moving boundary. As the present code is written to accommodate wall compliance, it is necessary to validate this code in test flows with moving boundaries. Unfortunately, there are very few fundamental test flows of this sort available in the literature for comparison. In previous work by our group, Luo & Bewley (2004) performed simulations of a laminar flow through a two-dimensional channel with an oscillating Gaussian bump using an (involved) contravariant formulation of the Navier-Stokes equation which is completely different from the present code (which is formulated with Cartesian vectors). We will use this result to validate the present code in the moving-boundary case.

Consider the laminar flow in a 2D channel with an oscillating Gaussian bump whose motion is prescribed by

$$\eta_l(x_1,t) = \varepsilon \sin(\omega t) \exp\left[-\frac{(x_1 - \frac{L_x}{2})^2}{\sigma^2}\right],$$

where  $\varepsilon$  is the maximum amplitude of the bump,  $\omega$  is the oscillation frequency, and  $\sigma$  is a constant parameterizing the length of the bump. The bump is uniform is the spanwise direction, so the laminar flow is two dimensional. In order to maintain incompressible flow, the upper wall is assumed to be penetrable and the normal velocity of the flow at the upper wall is taken to be identical to the vertical velocity of the lower wall. The simulation parameters are  $Re = \frac{U_c h}{V} = 200$ ,  $\varepsilon = 0.1$ ,  $\sigma = 0.2$ , where  $U_c$  is the centerline velocity. The domain size is  $L_x = L_z = \pi$  and the number of Fourier modes is  $42 \times 84 \times 4$  in the  $\xi_1$ ,  $\xi_2$ , and  $\xi_3$  directions, respectively.

Two simulation results are presented, one with slow wall motion,  $\omega = 0.5$ , and the other with faster wall motion,  $\omega = 4$ . In Figures 3 and 4, the instantaneous streamlines and pressure are compared with the results from Luo & Bewley (2004). As seen in Figures 3 and 4, in both simulations, the agreement between the two codes is excellent. Several symmetries

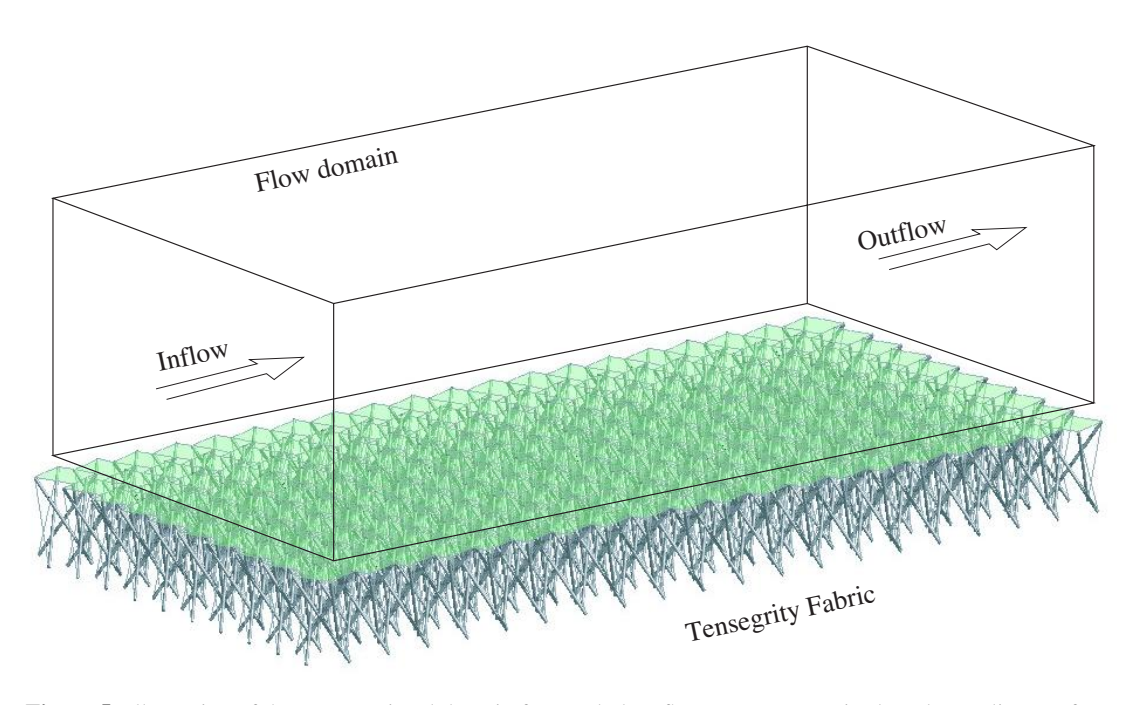


Figure 5. Illustration of the computational domain for a turbulent flow over a tensegrity-based compliant surface.

of the present (3D) code in the moving boundary case were also checked by aligning this (2D) flow and bump in various directions. For further discussion of the physics of this flow, see Luo & Bewley (2004).

#### 4. SIMULATION OF A TURBULENT FLOW OVER TENSEGRITY FABRICS

The geometrical configuration of the flow/structure system is shown in the Figure 5. All of the bars in the tensegrity fabric are assumed to be grounded. Discretized with the third-order Runge-Kutta scheme, the equation that governs dynamics of the compliant surface is coupled with (5), which governs dynamics of the flow, and is marched in time to simulate the interaction of the near-wall turbulence with the surface deformation. Two techniques have been identified to form the flow/structure interface between the (continuous) flow above and the (discrete) structure below. The first is to simply stretch a massless, tensionless and non-penetrable membrane over the top of the tensegrity structure, transmitting the force generated by the flow to the top nodes of the structure. Another option includes the attachment of small mechanical "scale" to each surface node of the tensegrity structure, mimicking the scales on a shark's skin. No-slip and no-penetration boundary conditions are assumed for the interface in either case. In our simulation model, we assume that the force from the flow is transmitted to the top nodes of the structure in a simple fashion approximating the latter technique. The surface is tessellated into small patches surrounding each node. The friction and pressure forces induced by the flow are then integrated over each patch and lumped to the associated node of the tensegrity structure. Since the bar nodes of the tensegrity structure do not coincide with the grid points in the flow model, the vertical displacements and velocities of the nodes are interpolated onto the uniform  $x_1 - x_3$  grid so they can be fed back to the flow system as the boundary condition.

In the flow/structure simulations, all velocities are normalized by  $u_{\tau}$  which is the viscous velocity from the corresponding regular channel flow with the same bulk mass flux. The Reynolds number for the flow is  $Re_{\tau} = u_{\tau}h/\nu = 150$ . (This corresponds to the Reynolds number based on the mean centerline velocity of the regular channel flow of  $Re = U_c h/\nu = 2663$ , and to the Reynolds number based on the bulk velocity of  $Re_b = U_{bulk}h/\nu = 2280$ .) The size of the computational domain is  $5.625\pi \times 2 \times \pi$ . That is, in wall units, the domain length and width are  $L_x^+ \approx 2651$  and  $L_z^+ \approx 471$ . The number of Fourier modes used is  $144 \times 94 \times 52$  in the  $\xi_1, \xi_2$ , and  $\xi_3$  directions respectively (i.e.,  $216 \times 94 \times 78$  dealiased collocation points). The tensegrity fabric used in the simulations consists of 45 unit cells in length and 8 cells in width, each of which has edge length of 0.36h and height of 0.51h (the height is taken to be twice of the radius of the cells). The fabric is pretensioned in such a manner that the tendons are about  $2 \sim 3$  times longer than their rest length.

For preliminary studies, we assume that all structural members have uniform material properties, i.e.,  $\rho_{b_i} = \rho_b$ ,  $\kappa_i = \kappa$  and  $\varsigma_i = \varsigma$ .

**Table 1**. Flow statistics for different tensegrity parameters.

case	$\rho_b$	κ	ς	$D_w$	$D_f$	$p_{w,rms}$	$v_{w,rms}$	$y_{w,max}^+$	$y_{w,rms}^+$	$p_w v_w$	$D_{form}$	TKE
I	0.08	0.10	0.05	1.00	0.99	1.5	0.007	0.45	0.12	-0.004	$4.7 \times 10^{-4}$	3.51
II	0.08	0.10	0.035	1.05	1.01	3.1	0.036	1.30	0.78	-0.084	0.014	3.64
III	0.08	0.10	0.03	1.17	1.03	5.0	0.069	2.38	1.00	-0.267	0.045	3.95
IV	0.08	0.06	0.05	1.01	1.02	1.6	0.008	0.63	0.18	-0.005	$6.0 \times 10^{-4}$	3.56
V	0.08	0.03	0.05	1.02	1.00	1.6	0.008	1.14	0.32	-0.005	$9.6 \times 10^{-4}$	3.55
VI	0.04	0.10	0.05	1.01	1.01	1.6	0.009	0.47	0.12	-0.007	$7.8 \times 10^{-4}$	3.55
VII	0.08	0.04	0.035	1.06	1.01	3.3	0.034	2.66	0.93	-0.070	0.013	3.75
VIII	0.08	0.04	0.03	1.22	1.05	5.9	0.078	5.34	1.94	-0.327	0.065	4.33
regular channel				1	1	1.45	0	0	0	0	0	3.52

#### 5. RESULTS

A fully-developed turbulent flow in a regular channel (with solid walls) is used as the initial condition for all of the compliant channel flows studied. After making the walls compliant and allowing the transient in the flow to settle, flow statistics are gathered over sufficiently long time intervals to achieve statistical convergence. Table 1 shows selected flow statistics for some various combinations of tensegrity parameters, along with the statistics of the flow in the regular channel with the same bulk velocity. The statistics reported are the total drag  $D_w$  on the compliant wall, the drag on the flat wall  $D_f$ , the root mean-square (rms) of the compliant wall pressure  $p_{w,rms}$ , the rms wall velocity  $v_{w,rms}$ , the maximum wall deformation  $y_{w,rms}^+$ , the rms of the wall deformation  $y_{w,rms}^+$ , the power done on the flow by wall pressure  $p_w v_w$ , the form drag on the compliant wall  $D_{form}$ , and the turbulent kinetic energy (TKE) in the channel.

When the structure is stiff with high damping (e.g., case I, where  $\rho_b = 0.08$ ,  $\kappa = 0.10$  and  $\zeta = 0.05$ ), the compliant surface barely changes the flow statistics. In case I, the wall deformation and the wall velocity are both very small, and the flow behaves as if the interface were a solid, flat wall. When the structural damping is reduced, as in case II and III where  $\zeta = 0.035$  and  $\zeta = 0.03$ , respectively, the interface starts to move more and the flow statistics are changed significantly. The total drag on the interface is increased by 5% in case II and 17% in case III, and the TKE is increased by 3% and 12% respectively. In next section, we will show that these changes are caused by the resonant vibration of the compliant structure.

In case IV and V, we keep the damping  $\varsigma = 0.05$ , but reduce the tendon stiffness  $\kappa$  to 0.06 and 0.03, respectively. The flow statistics are slightly modified. The wall deformation grows as the the structure gets softer. However, the wall does not move much faster than in case I due to high system damping. In case VI, we reduce the bar density  $\rho_b$  to 0.04. Not surprisingly, the potential influences of external disturbances and its own restoring forces on this lighter structure are counteracted by the increased effect of internal damping, so the flow is again not affected much by the surface compliance.

Case VII and VIII have both the stiffness and damping lowered. In case VII, where  $\kappa=0.04$  and  $\varsigma=0.035$ , the instantaneous wall deformation reaches 5 viscous units, and in case VIII, where  $\kappa=0.04$  and  $\varsigma=0.03$ , it reaches 9 viscous units. The flow statistics are greatly affected by the surface compliance. The total drag on the interface is increased by 6% in case VII and 22% in case VIII, and the TKE is increased by 7% and 23% respectively in the two cases. We distinguish these two cases from case II and III because, although case VII and VIII have larger wall deformations, the motion of the surface is less synchronized than it is in cases II and III. The present article thus focuses on cases II and III; the other cases are discussed in greater detail in Luo & Bewley (2005).

Interestingly, in all of the cases in the present work in which the flow statistics are significantly modified by the wall compliance, the deformation of the wall is dominated by spanwise ridges that travel in the streamwise direction, reminiscent of an air/water interface forced by the wind, as discussed in Fulgosi *et al.* (2003). Note however that the waves on the interface considered in Fulgosi *et al.* travel at a much slower phase speed than in the present work and have no significant influence on the overlying air flow. This section investigates some additional details of the flow/structure interaction in cases II and III, in which the wall seems to resonate under the excitation of the overlying turbulent flow fluctuations, which in term excites further fluctuations in the turbulent flow.

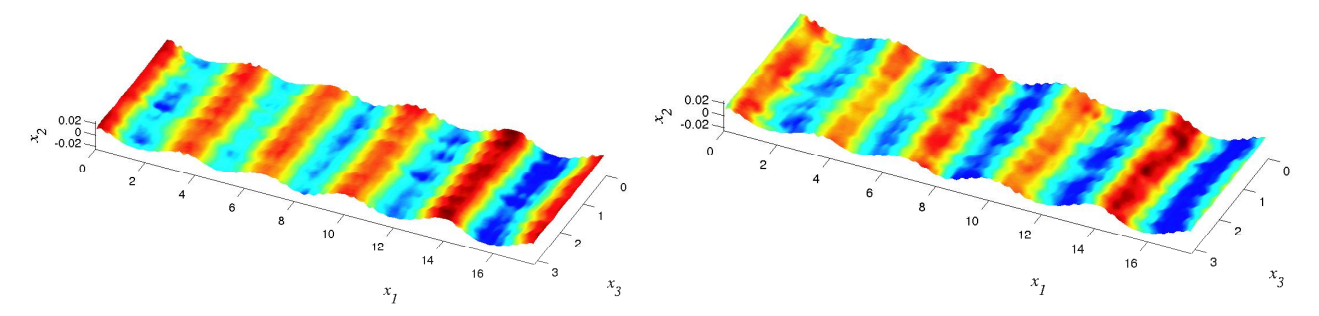


Figure 6. Visualization of the flow/structure interface in case III. Left: wall displacement from its nominal position  $x_2 = -1$ ; right: wall velocity.

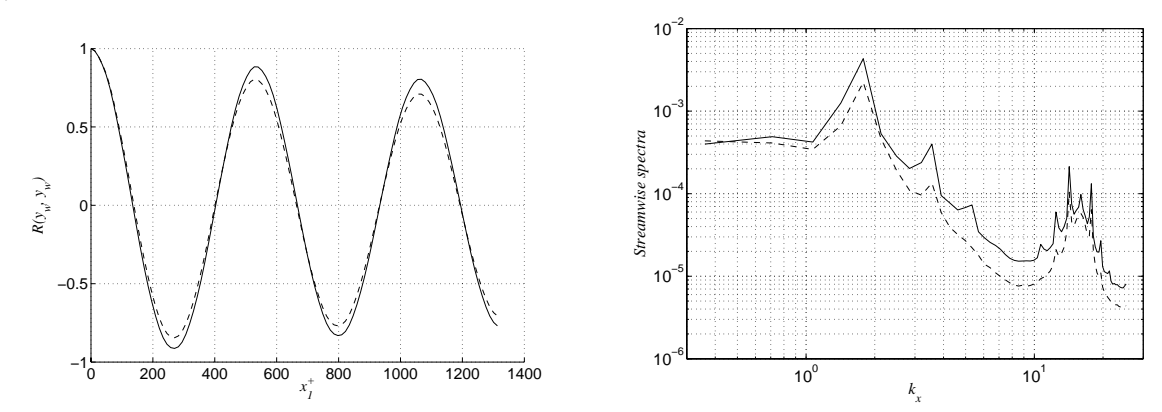


Figure 7. Spatial characteristics of the wall deformation  $y_w$  for case II (dashed) and case III (solid). Left: streamwise autocorrelation; right: streamwise spectra in log-log scale.

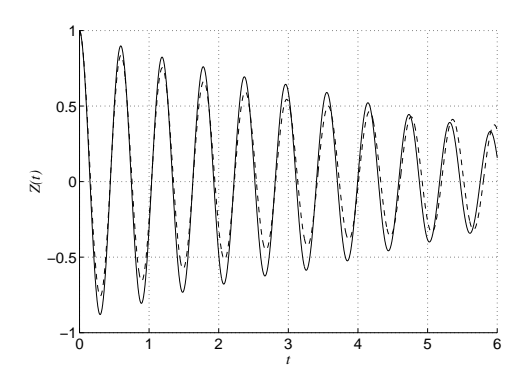
Figure 6 depicts the shape and velocity of the interface at an instant moment for case III. The wall deformation is approximately sinusoidal in the streamwise direction, and the wall velocity has about 90° phase shift ahead of the wall, indicating that the wave is traveling in the same direction as the flow. Case II has the similar wall deformation with a smaller interfacial wave amplitude.

The wavelength,  $\lambda$ , of the interfacial motion may be seen from the statistics of the streamwise two-point correlation function\* of the wall displacement,  $R(y_w, y_w)$ , as plotted in Figure 7(a). The minimum of the first valley may be interpreted as the half wavelength. For cases II and III, we find that  $\lambda^+ = 530$ . The correlation functions also indicate that the interface in case III has a more regular sinusoidal shape, as its autocorrelation decays more slowly than in case II. In the streamwise spectra of wall deformation (Figure 7(b)), the corresponding vibration mode for both cases,  $k_x = 1.78$ , is much stronger than the other modes. The "hump" in the region  $k_x > 10$  is related to the response of the wall to small-scale perturbations in the flow. The "spikes" in this region coincide with the geometrical length scales of the tensegrity cells, and are thus related to the discrete nature of the tensegrity structure.

The time correlation function of a fixed point on the wall, Z(t), and the time spectra of wall oscillations of the two cases, are shown in Figure 8. From them we may estimate the period,  $t_p = 0.6$ , and frequency,  $f_{freq} = 1.6$ , of the resonance. The phase speed of the travelling wave is thus  $c/u_{\tau} = \lambda/t_p \approx 6$ .

Instantaneous pressure disturbances on the wavy interface are visualized in Figure 9(a). As opposed to turbulence over a stationary wavy wall, where the pressure peaks on the upstream side of the wave and reaches to minimum near the wave crests, the pressure in the present case, with a streamwise-travelling wave on the surface, has its minimum on the downstream side of the wave crests, causing this portion of the wall to elevate, thereby sustaining the wave motion.

<sup>\*</sup>The normalized spatial correlation function of two quantities, f and g, is defined by  $R_{fg}(\mathbf{r}) = \frac{\langle f(\mathbf{x})g(\mathbf{x}+\mathbf{r}) \rangle}{\sqrt{\langle ff \rangle \langle gg \rangle}}$ 



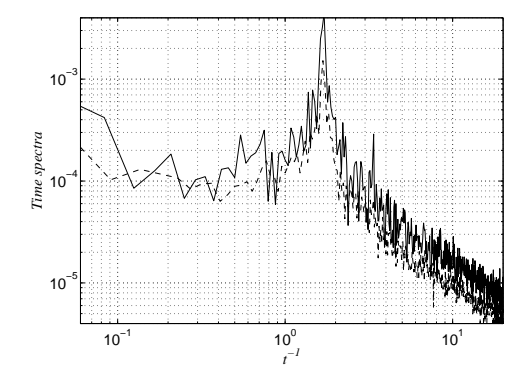


Figure 8. Temporal characteristics of the wall deformation  $y_w$  for case II (dashed) and case III (solid). Left: time autocorrelation; right: time spectra in log-log scale.

The resulting "adverse pressure gradient" slows down the flow and therefore reduces the shear stress on downstream side, sometimes even causing flow separation (Figure 9(b)). The deformation of the compliant wall has a maximum wave slope given by  $y_w k_x = 0.027$ . This slope is comparable to deformation of the air-water interface reported in Fulgosi *et al.* (2003), where it was found that, at a shear Reynolds number  $Re_{\tau} = 171$ , the slow interface motion of an air/water interface has only slight effects on the air flow near the interface. In contrast, in the present system, significant changes to the turbulent flow statistics are excited by the resonant wall motion.

The near-wall quasi-streamwise vorticies have been strengthened due to the interfacial motion in the present simulations. To visualize this, Figure 10 depicts isosurfaces of the discriminant field, a scalar quantity derived from the velocity gradient tensor and providing a handy identification technique for identifying "vortex-type" motions in a near-wall turbulent flow. The deformation of the wall is indicated by the colors on the surface. It is seen that the vorticies are more concentrated above the valleys.

The deformed tensegrity fabric in case III is visualized in detail in Figure 11, where it can be seen that the amplitude of the flow/structure interface displacement is only about 3% of the fabric height in this case.

Profiles of the rms value of the velocity and pressure fluctuations, the Reynolds stresses, and the mean velocity in case III are given in Figure 12, together with the corresponding profiles in regular channel-flow turbulence at the same bulk Reynolds number. Note that the lower wall is a moving deformed surface, and that statistics are gathered from surfaces on which  $\xi_2$  is constant. When the wall deformation is small, these surfaces are approximately locally parallel to the wall. Near the lower wall, the flow disturbances are increased significantly due to the wall compliance;  $u_{2,rms}$  and  $u_{3,rms}$  are more than 20% higher, and  $u_{1,rms}$  is slightly higher, than in the regular turbulent channel flow. The Reynolds stress,  $-\langle u_1 u_2 \rangle$ , is also much larger in this region, indicating that TKE production is significantly increased. Near the flat wall, the flow disturbances are barely modified, indicating that compliance of the lower wall has little influence on the turbulence statistics near the upper wall. However, the profile of the mean streamwise velocity,  $\langle u_1 \rangle$ , is distorted on both sides of the channel, with reduced velocity near the lower wall and increased velocity near the upper wall. The mean velocity is significantly impeded by the high drag on the compliant wall; note that the mean velocity must increase elsewhere in the channel flow to compensate, as the overall pressure gradient must be increased in this case to insure that the constant mass flux constraint on the flow is satisfied.

The two-point correlations of the velocity fluctuations  $R_{u_\kappa u_\kappa}(x_1)$  and  $R_{u_\kappa u_\kappa}(x_3)$  in the near-wall region ( $\xi_2^+ = 5.6$ ) for case III are illustrated in Figure 13. Near the wall, the correlations of the velocity fluctuations are modified substantially by the wall compliance:  $R_{u_\kappa u_\kappa}(x_1)$  monotonically decreases with  $x_1$  near the wall in the regular channel case, but fluctuates above and below zero due to the sinusoidal wall deformation in case III. The wavelength of this correlation is the the same as the wavelength of the surface deformation. The spanwise correlations near the wall are "raised" due to the spanwised-synchronized vertical motion of the boundary, which is nearly uniform in the  $x_3$  direction. However, the characteristic spanwise length scales (that is, the distance to the first minimum points) of the turbulent flow fluctuations near the wall (that is, the coherent structures) seem to be relatively unaffected by the wall motion. Though not shown here, the wall motion has relatively little influence on the velocity correlations near the channel center.

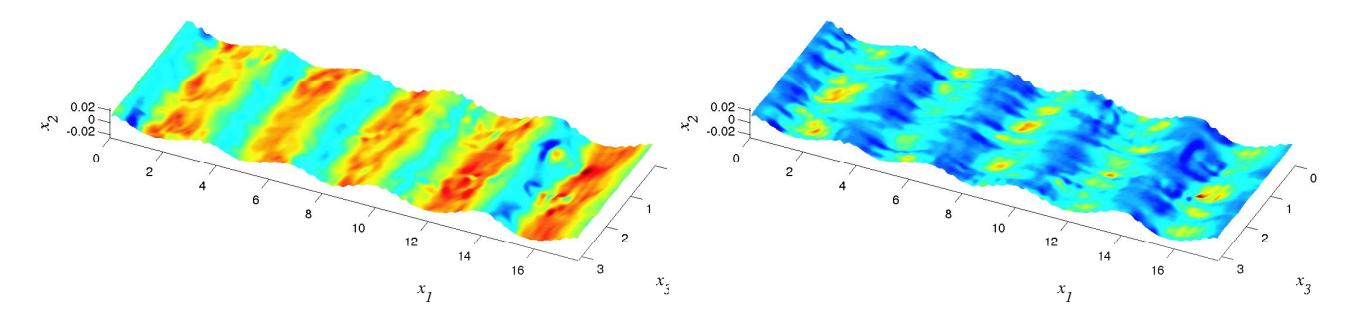
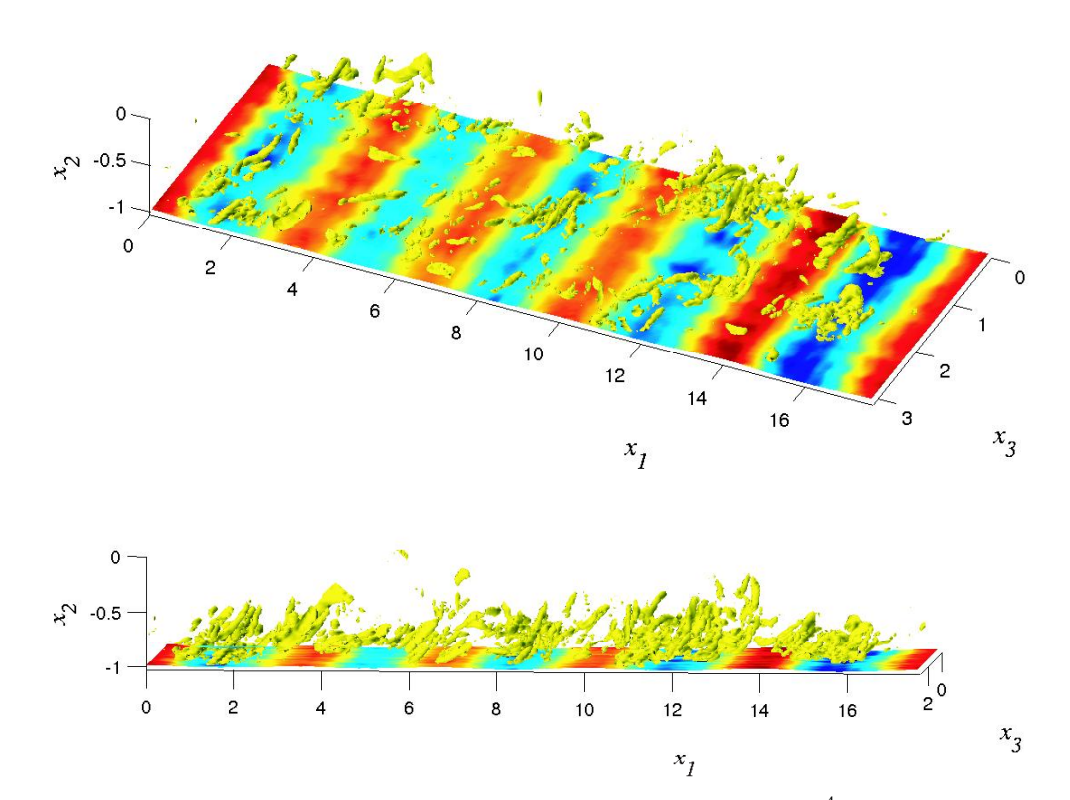
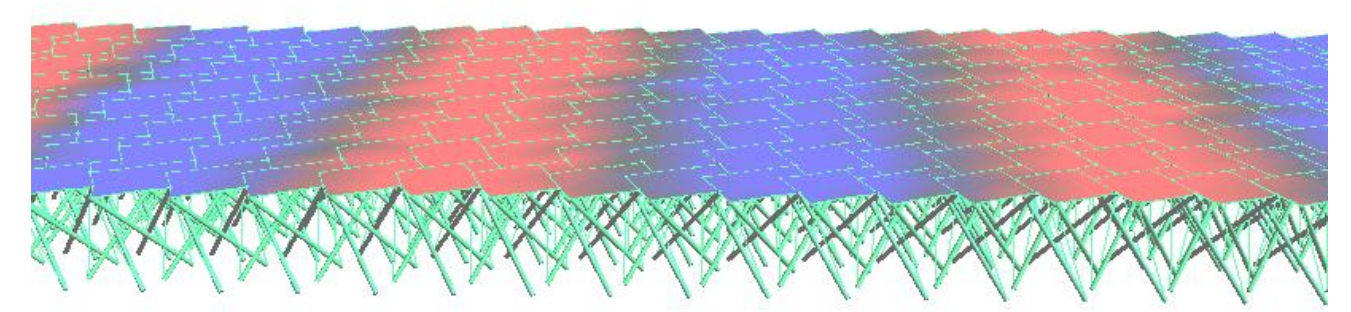


Figure 9. Instantaneous wall pressure (left) and streamwise shear stress (right) on the interface in case III.



**Figure 10.** Two different views of the discriminant of the flow in case III at the isosurface level  $10^{-4}$ . The colors on the interface indicate the amplitude of the interface deformation.



**Figure 11.** Close-up view of the streamwise-travelling wave induced on the tensegrity fabric by the overlying turbulent flow (going from left to right). Red denotes elevation of the surface, and blue denotes depression of the surface.

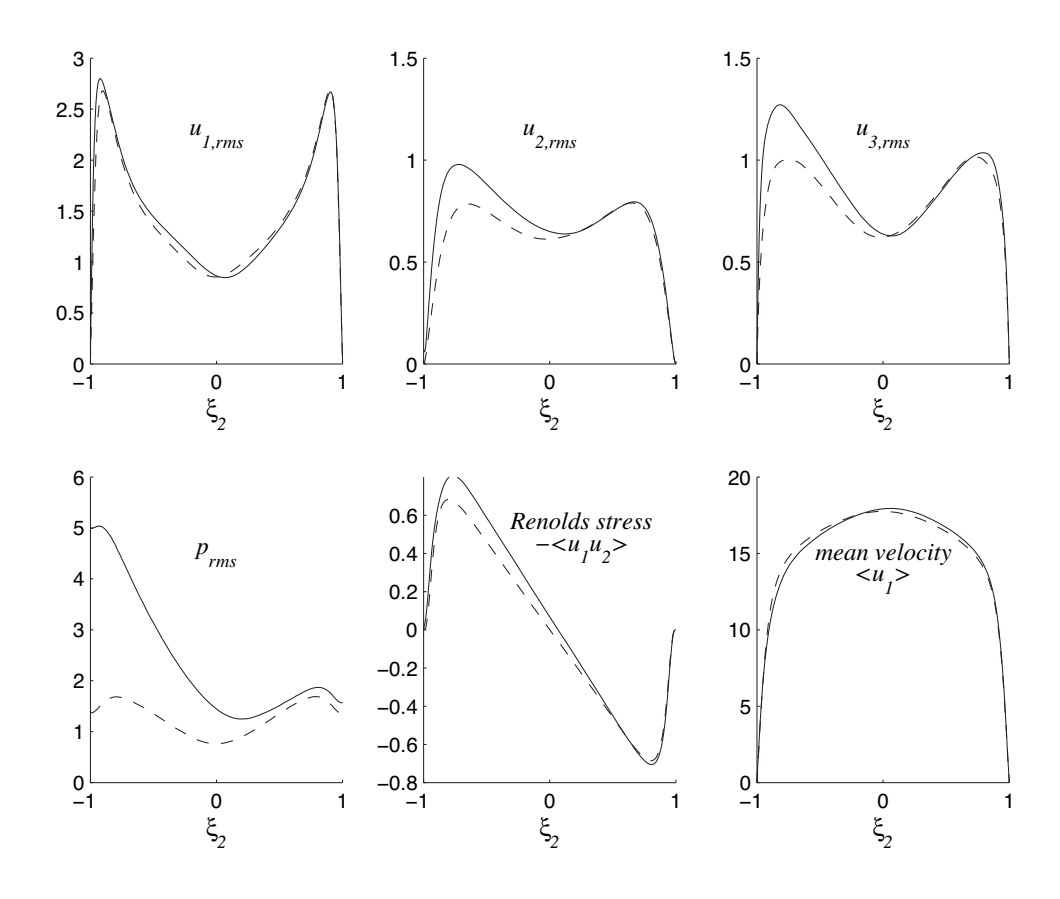


Figure 12. Profiles of the flow field for case III. Dashed: statistics from the regular channel flow; solid: statistics from the compliant channel.

#### 6. CONCLUDING REMARKS

The ultimate goal of this research project is to study and optimize a new type of compliant material, dubbed a *tensegrity fabric*, for the possible mitigation of the drag induced by near-wall turbulence. The present paper discussed the accurate computational modeling of the delicate interaction of a turbulent flow (at relatively low Reynolds number) and the tensegrity fabric and characterized the significant effects of this interaction on the statistics of the near-wall turbulence.

Unlike a spring/plate surface model of a compliant surface, to which a turbulent flow does not seem to be particularly sensitive, the tensegrity-based compliant surface demonstrates a significant influence on the statistics of near-wall turbulence. This paper performed a preliminary parametric study of three important material parameters defining the compliance properties of the fabric: specifically, the density, stiffness, and damping of the members of the tensegrity structure. Simulations illustrated that, when the structure's stiffness and damping are low, the interface forms a streamwise traveling wave resembling that at an air-water interface, but convecting with a much higher phase velocity. For some combinations of the tensegrity parameters, the compliant wall demonstrated a resonant oscillation as a result of the excitation by the turbulent flow. The wavy motion of the interface in the simulations performed caused large *increases* of the drag and turbulent kinetic energy of the flow. Shear stress was found to account for the major portion of the overall drag. Appropriate grid refinement and computational domain size checks were performed to insure that neither numerical resolution nor computational domain size had a significant influence on the statistics reported.

This work is, as far as we know, the first computational study of the turbulent flow / compliant surface problem to both resolve accurately the system under consideration and demonstrate a significant effect of a compliant surface on the statistics of near-wall turbulence. Unfortunately, the parameter regime studied turned out to exhibit drag-increasing properties. Besides the spanwise-synchronized travelling waves on the of the flow/structure interface, as reported in this paper, we have also seen (e.g., in case V) that the interface may form small, approximately streamwise-synchronized

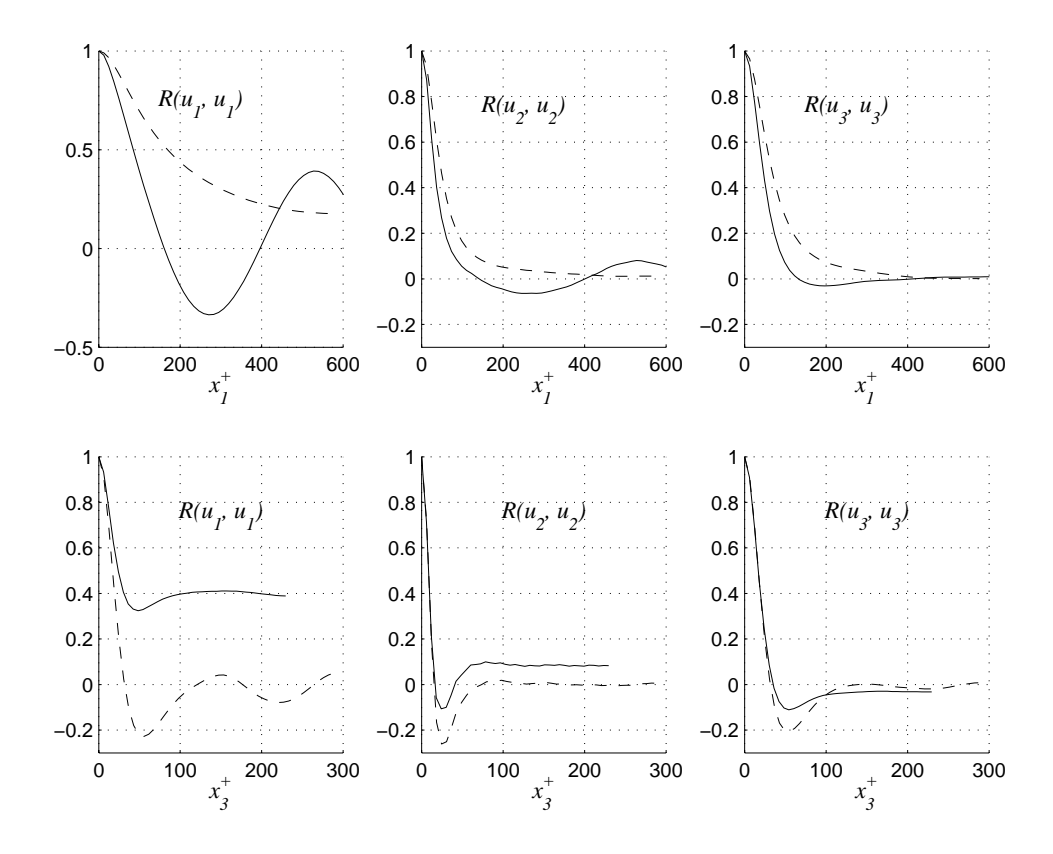


Figure 13. Streamwise (upper row) and spanwise (lower row) two-point correlations of velocities at  $x_2^+ = 5.6$  for case III. Dashed: statistics from the regular channel flow; solid: statistics from the compliant channel.

ridges. Tuning the parameters to further enhance such ridges might be a profitable approach to take, as it is known that stationary streamwise "riblets" of the appropriate size have a significant drag-reducing effect (Choi *et al.*, 1993), and that active spanwise oscillations of the wall can also reduce drag (Jung *et al.*, 1992).

The tensegrity fabric has extensive design flexibility that remains, as yet, largely unexplored, including the modification of the tensegrity cell's geometry in addition to the individual material properties of each structural elements within a cell. Future optimization work within this large parameter space might thus possibly stumble upon a fabric with favorable (that is, drag reducing) properties. Note that the software that simulates the dynamics of the flow/structure system couples an involved Fortran90 code, which calculates accurately and efficiently a turbulent flow with a flexible boundary using a time-dependent coordinate transformation, with an involved C++ code, that calculates accurately and efficiently the dynamics of a large, interconnected array of structural elements. The flow simulations reported in this paper contained  $7 \times 10^{-5}$  grid points, and the structural simulations performed contained 1440 bars and 3653 tendons. A typical simulation to calculate the time-averaged turbulence statistics of a particular configuration of the tensegrity fabric takes about a day of dedicated simulation time on an 8-CPU IBM P655 node. Thus, an efficient optimization strategy will be essential to the ultimate success of this project and its scaling to higher Reynolds numbers.

# **ACKNOWLEDGMENTS**

The authors gratefully acknowledge the funding by the DARPA Synthetic Multifunctional Materials Program (Dr. Leo Christodoulou) and the ONR Young Investigator Program (Dr. Ron Joslin), which made this work possible.

# References

BENJAMIN, T. 1960 Effects of a flexible boundary on hydrodynamic stability. J. Fluid Mech. 9, 513-532.

- BEWLEY, T. & PROTAS, B. 2004 Skin friction and pressure: the "footprints" of turbulence. Physica D 196, 28-44.
- BEWLEY, T. R., MOIN, P. & TEMAM, R. 2001 DNS-based predictive control of turbulence: an optimal benchmark for feedback algorithms. *J. Fluid Mech.* 447, 179–225.
- BUSHNELL, D., HEFNER, J. & ASH, R. 1977 Effect of compliant wall motion on turbulent boundary layers. *Phys. Fluids A* 20 (10), S31–48.
- CARPENTER, P., DAVIES, C. & LUCEY, A. 2000 Hydrodynamics and compliant walls: Does the dolphin have a secret? *Current Science* **79**, 758–765.
- CARPENTER, P. & GARRAD, A. 1985 The hydrodynamic stability of flow over Kramer-type compliant surfaces. I. Tollmien-Schlichting instabilities. *J. Fluid Mech.* **155**, 465–510.
- CARPENTER, P. & MORRIS, P. 1990 The effect of anisotropic wall compliance on boundary-layer stability and transition. *J. Fluid Mech.* 218, 171–223.
- CHOI, H., MOIN, P. & KIM, J. 1993 Direct numerical simulation of turbulent flow over riblets. J. Fluid Mech. 255, 503-539.
- CHOI, K.-S., X., Y., CLAYTON, B., GLOVER, E., ATLAR, M., SEMENOV, B. & KULIK, V. 1997 Turbulent drag reduction using compliant surfaces. *Proc. Royal Soc. Lond. A* 453, 2229–2240.
- DANIEL, A., GASTER, M. & WILLIS, G. 1987 Boundary layer stability on compliant surfaces. *Tech. Rep.* Final Report No. 35020. British Maritime Technology Ltd., Teddington, Great Britain.
- DAVIES, C. & CARPENTER, P. 1997 Numerical simulations of the evolution of Tollmien-Schlichting waves over finite compliant panels. *J. Fluid Mech.* 335, 361–392.
- ENDO, T. & HIMENO, R. 2002 Direct numerical simulation of turbulent flow over a compliant surface. J. Turbulence 3 (007), 1–10.
- FULGOSI, M., LAKEHAL, D., BANERJEE, S. & ANGELIS, V. D. 2003 Direct numerical simulation of turbulence in a sheared air-water flow with a deformable interface. *J. Fluid Mech.* **482**, 319–345.
- GASTER, M. 1988 Is the dolphin a red herring? In *Turbulence management and relaminarisation* (ed. H. Liepmann & R. Narasimha), pp. 285–304. Berlin: Spinger.
- GAD-EL HAK, M. 1986 The response of elastic and viscoelastic surfaces to a turbulent boundary layer. J. Appl. Mech. 53, 206-212.
- GAD-EL HAK, M. 1987 Compliant coatings research: a guide to the experimentalist. J. Fluids Struct. 1, 55-70.
- GAD-EL HAK, M. 1996 Compliant coatings: a decade of progress. Appl. Mech. Rev. Part 2 49 (10), S1-11.
- INGBER, D. E. 1997 Tensegrity: The architectural basis of cellular mechanotransduction. Annual Review of Physiology 59, 575–599.
- INGBER, D. E. 1998 Architecture of life. Scientific American January, 48–57.
- JUNG, W. J., MANGIAVACCHI, N. & AKHAVAN, R. 1992 Suppression of turbulence in wall-bounded flows by high-frequency spanwise oscillations. *Phys. Fluids A* **4**, 1605–1607.
- LANDAHL, M. 1962 On the stability of a laminar incompressible boundary layer over a flexible surface. J. Fluid Mech. 13, 609-632.
- LEE, T., FISHER, M. & SCHWARZ, W. 1993 Investigation of the stable interaction of a passive compliant surface with a turbulent boundary layer. *J. Fluid Mech.* **257**, 373–401.
- LUO, H. & BEWLEY, T. 2003 Design, modeling, and optimization of compliant tensegrity fabrics for the reduction of turbulent skin friction. SPIE Paper (5049-57).
- LUO, H. & BEWLEY, T. 2005 Modelling and simulation of turbulence over a tensegrity fabric type compliant surface. Submitted, *J. Fluid Mech.*
- Luo, H. & Bewley, T. R. 2004 On the contravariant form of the Navier-Stokes equation in time-dependent curvilinear coordinate systems. *J. Comput. Phys.* **199** (1), 355–375.
- ROSENFELD, M. & KWAK, D. 1991 Time-dependent solutions of viscous incompressible flows in moving co-ordinates. *Int. J. Numerical Methods in Fluids* 13, 1311–1328.
- Xu, S., Rempfer, D. & Lumley, J. 2003 Turbulence over a compliant surface: numerical simulation and analysis. *J. Fluid Mech.* 478, 11–34.